PHOTONICS Research

Faster structured illumination microscopy using complementary encoding-based compressive imaging

ZHENGQI HUANG,[1] YUNHUA YAO,[1,5] (iD) YILIN HE,[1] YU HE,[1] CHENGZHI JIN,[1] MENGDI GUO,[1] DALONG QI,[1] (iD) LIANZHONG DENG,[1] ZHENRONG SUN,[1] ZHIYONG WANG,[2,6] AND SHIAN ZHANG[1,3,4,7] (iD)

[1]State Key Laboratory of Precision Spectroscopy, School of Physics and Electronic Science, East China Normal University, Shanghai 200241, China
[2]School of Mathematical Sciences, University of Electronic Science and Technology of China, Chengdu 611731, China
[3]Joint Research Center of Light Manipulation Science and Photonic Integrated Chip of East China Normal University and Shandong Normal University, East China Normal University, Shanghai 200241, China
[4]Collaborative Innovation Center of Extreme Optics, Shanxi University, Taiyuan 030006, China
[5]e-mail: yhyao@lps.ecnu.edu.cn
[6]e-mail: zhywang@uestc.edu.cn
[7]e-mail: sazhang@phy.ecnu.edu.cn

Structured illumination microscopy (SIM) has been widely applied to investigate intricate biological dynamics due to its outstanding super-resolution imaging speed. Incorporating compressive sensing into SIM brings the possibility to further improve the super-resolution imaging speed. Nevertheless, the recovery of the super-resolution information from the compressed measurement remains challenging in experiments. Here, we report structured illumination microscopy with complementary encoding-based compressive imaging (CECI-SIM) to realize faster super-resolution imaging. Compared to the nine measurements to obtain a super-resolution image in a conventional SIM, CECI-SIM can achieve a super-resolution image by three measurements; therefore, a threefold improvement in the imaging speed can be achieved. This faster imaging ability in CECI-SIM is experimentally verified by observing tubulin and actin in mouse embryonic fibroblast cells. This work provides a feasible solution for high-speed super-resolution imaging, which would bring significant applications in biomedical research. © 2024 Chinese Laser Press

1. INTRODUCTION

With the spatial resolution beyond the optical diffraction limitation, super-resolution microscopy has been widely applied in the observation of the fine structures and dynamics in cells, which has greatly boosted the development of the biomedical field. Several super-resolution fluorescence microscopy techniques have been proposed based on various principles [1], which provide multiple options. Notable examples include stimulated emission depletion microscopy (STED) based on point spread function narrowing [2–4], single molecule localization microscopy (SMLM) utilizing localization of photo-switchable fluorescence molecules [5,6], and structured illumination microscopy (SIM) employing spatial frequency shifting [7–9]. Due to the unique advantages of high imaging speed, low photo damage, and wide applicability for fluorescence labels, SIM has emerged as the most widely used super-resolution microscopy technique for studying the structure of living biological cells, such as actin

cytoskeleton [10], mitochondria [11], lysosomes [12], and endoplasmic reticulum [13].

However, limited by the requirement for nine measurements with different structured patterns, the imaging speed of SIM is restricted by the frame rate of the deployed camera. Besides, it is difficult to further improve the frame rate of a camera with a sufficiently large bit depth and a high pixel resolution. Although video-rate super-resolution imaging has been achieved in SIM, it is still unable to observe the high-speed dynamics of fine structures. To further improve the super-resolution imaging speed of SIM, various methods have been proposed. Some methods aimed to reduce the number of images required for SIM reconstruction by exploiting the information redundancy [14]. For example, SIM reconstruction with only four images was achieved by various algorithms, including the Bayesian framework, the least squares method, and the modified incoherent Fourier ptychographic procedure [15–17].

A deep-learning-based SIM reconstruction algorithm with three images was proposed by leveraging the isotropy of the fluorescence [18]. However, the information redundancy is sometimes disturbed by the noise, which leads to a poor quality in the reconstructed super-resolution images. Some other methods aimed to compress multiple raw images to fewer measurements with compressive sensing (CS). For example, CS-based frameworks were developed to reconstruct super-resolved images with fewer pixels or downsampling [19,20]. Although these works reduced the collected information, no improvement in the imaging speed was obtained. Introducing a snapshot compressive imaging conception into SIM is a potential strategy to accelerate the super-resolution imaging [21]. A compressed imaging-based SIM technique (CISIM) was proposed to improve the imaging speed by compressing multiple raw images into only one recorded image and subsequently extracting the super-resolution images, as reported in our previous work [22]. However, different from conventional imaging, the precise recovery of the high-frequency information with structured illumination from compressed measurements remains challenging due to the high data compression ratio and the high noise sensitivity. Moreover, precise structured illumination patterns are required for a reconstruction in CISIM, which are difficult to acquire in the experiment from the compressed measurements. These issues hinder the implementation of CISIM in the real observation of high-speed biomedical dynamics.

To solve these issues, here we report a structured illumination microscopy with complementary encoding-based compressive imaging, termed CECI-SIM. CECI-SIM integrates complementary encoding-based temporal compressive imaging (TCI) with SIM to elevate the super-resolution imaging speed. By encoding every three raw images with the illumination patterns of different phase-shift steps in the same direction with complementary codes and compressing them into a single image, only three compressed images are required for the reconstruction of a super-resolution image in CECI-SIM. The complementary encoding strategy effectively alleviates the recovery burden of the fine structural information from the compressed images. A high-performance image reconstruction algorithm is developed to reconstruct the super-resolution

images, which consists of a reconstruction algorithm based on the alternating direction method of multipliers (ADMM) for temporal compressive imaging (TCI) reconstruction and a HiFi-SIM algorithm for SIM reconstruction. The faster super-resolution imaging ability of CECI-SIM is demonstrated experimentally by the observations of tubulin and actin in mouse embryonic fibroblast cells, which shows a close performance in the image quality with conventional SIM and a three-fold imaging speed improvement. Given the powerful ability in the super-resolution imaging speed, CECI-SIM can provide a potential tool for the investigation of high-speed intracellular dynamics.

2. THEORETICAL MODEL

Conventional SIM necessitates nine raw images with illumination patterns involving three phase-shift steps in three directions. Three phase shifts in every direction are utilized to precisely calculate the zeroth-order low-frequency components and the first-order high-frequency ones, while the illumination patterns of the three directions are used to obtain the isotropic super-resolution images. Consequently, the super-resolution imaging speed of conventional SIM can only reach 1/9 of that of the recording camera. In other words, the imaging speed bottleneck of conventional SIM lies in the frame rate of the camera. Since it is difficult to further improve the frame rate of a camera with sufficient bit depth and pixel number, compressing multiple raw images under the limited frame rate of the camera is a potential strategy. Based on the compressive sensing theory [23–25], the sparsity in natural fluorescence images and the uncorrelated sampling offer a precondition for the recovery of the compressed images.

The schematic diagram of CECI-SIM is shown in Fig. 1, which consists of two parts: image acquisition and image reconstruction. In the image acquisition part, illumination light with nine structured patterns $p(x, y, n)$ is periodically projected onto the fluorescently labeled sample $d(x, y)$ to produce spatial frequency shifting, where the nine structured patterns are assigned in three directions and three phase-shift steps. Therefore, a series of nine structured fluorescent images are
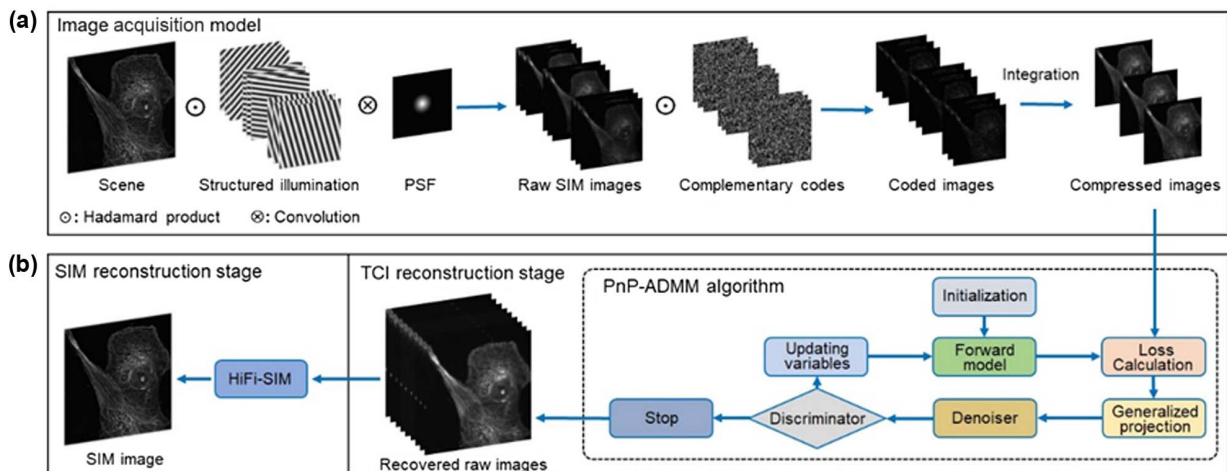

Fig. 1. Schematic diagram of CECI-SIM. (a) The image acquisition part of CECI-SIM. (b) The image reconstruction part of CECI-SIM.

generated, which contain the super-resolution information in different directions. After passing through an objective lens, the acquired raw SIM images $s(x, y, n)$ can be considered as the convolution of the structured fluorescent images with the point spread function (PSF) $h(x, y)$ of the objective lens according to the optical diffraction, which can be written as

$$s(x, y, n) = \iint h(\tau_x - x, \tau_y - y)p(x, y, n)d(x, y)\mathrm{d}x\mathrm{d}y. \quad (1)$$

In conventional SIM, the raw SIM images $s(x, y, n)$ are directly recorded by a camera to reconstruct the super-resolution images. However, these raw SIM images in CECI-SIM are further modulated by complementary pseudorandom binary codes $c(x, y, t)$. As shown in Fig. 1(a), every three raw images with illumination patterns in the same direction while different phase-shift steps are modulated with three complementary pseudorandom binary codes and then integrated into a compressed image, which is recorded by a camera in a single exposure. Thus, nine raw SIM images are compressed into a total of three images. Every single recorded image of the three raw images $m(x, y, t)$ can be expressed as

$$m(x, y, t) = \int c(x, y, t)s(x, y, n)\mathrm{d}n. \quad (2)$$

The three binary codes have complementary distribution, which means the value of their summation in every pixel is equal to l. With these special complementary codes, the recovery from the compressed measurement has higher fidelity [26]. For simplification, the image acquisition of CECI-SIM can be rewritten with a matrix form and is given by

$$\boldsymbol{m} = IC\boldsymbol{s} = A\boldsymbol{s}, \quad (3)$$

where $\boldsymbol{m}$ is the matrix of the compressed images $m(x, y, t)$, C represents the encoding operator with the spatial modulation $c(x, y, t)$, and I represents the integral operator with the camera. The whole optical transfer operator of CECI-SIM can be simplified as A.

To obtain the super-resolution image from the compressed images in CECI-SIM, an image reconstruction algorithm with two stages is designed, which consists of TCI reconstruction and SIM reconstruction, as shown in Fig. 1(b). For the TCI reconstruction, an iterative algorithm based on ADMM framework is utilized to recover the raw SIM images from the recorded compressed ones [27–29]. Since it has a plug-and-play (PnP) structure with replaceable priors [30,31], it is abbreviated to PnP-ADMM. The inverse problem of the TCI reconstruction can be described mathematically as

$$\hat{\boldsymbol{s}} = \underset{\boldsymbol{s}}{\arg\min}\|\Phi\boldsymbol{s}\|_1, \text{ subject to } A\boldsymbol{s} = \boldsymbol{m}, \quad (4)$$

where Φ is the transformation operator of a sparse domain, and $\|\cdot\|_1$ denotes the L$_1$ norm. Considering maximum likelihood estimation [32], the optimization problem can be solved iteratively and is given by

$$\begin{cases} \boldsymbol{s}^{(k+1)} = (\boldsymbol{v}^{(k)} - \boldsymbol{u}^{(k)}) + \frac{1}{\rho}A^T(I + \frac{1}{\rho}AA^T)^{-1}[\boldsymbol{m} - A(\boldsymbol{v}^{(k)} - \boldsymbol{u}^{(k)})] \\ \boldsymbol{v}^{(k+1)} = D_\Phi(\boldsymbol{s}^{(k+1)} + \boldsymbol{u}^{(k)}) \\ \boldsymbol{u}^{(k+1)} = \boldsymbol{u}^{(k)} + (\boldsymbol{s}^{(k+1)} - \boldsymbol{v}^{(k+1)}) \end{cases}, \quad (5)$$

where $\boldsymbol{v}$ and $\boldsymbol{u}$ are the auxiliary intermediate variables of ADMM, ρ is a scale factor of ADMM, and D_Φ is the denoiser with priors. As shown in Fig. 1(b), the flow chart of the PnP-ADMM algorithm is described as follows. A set of random images are set as the initialized iterative variable in the iterative algorithm. First, the current expectation of a compressed image for the iterative variable is estimated based on the image acquirement process in CECI-SIM, which can be measured in the system calibration. Second, the loss between the current expectation and the real measured value of CECI-SIM is calculated. Third, the generalized projection method automatically optimizes the iterative variable based on the loss value above. Fourth, the result from the gradient descent search is filtered with image denoisers that satisfy some kind of sparse constraint. Finally, the discriminator will judge the convergence status of the algorithm. If the residual between the last iterative variable and the new one is below the threshold value, the iterative algorithm will stop and output the reconstruction result. Otherwise, the algorithm will continue the next iterative search. Thus, nine raw SIM images are reconstructed from three compressed images through TCI reconstruction. Benefiting from the PnP framework, the image denoisers with different priors can be flexibly switched in the algorithm. In this work, total variation (TV) and DRUNet denoisers are jointly utilized [30,33], which, respectively, explore the total variation minimization and deep-learning-based image priors to ensure that the recovered results have high enough signal-to-noise ratios (SNRs) and retain the high-frequency image details for further SIM reconstruction.

Regarding the SIM reconstruction stage in CECI-SIM, conventional SIM algorithms can be used to solve the task [34,35]. However, a SIM reconstruction algorithm with high robustness to input raw images is desired because some image degradations occur during the reconstruction from compressed images in the previous stage. Thus, here the HiFi-SIM algorithm is employed in this work due to its excellent suppression of artifacts and noise [36].

3. SIMULATION RESULTS

To assess the feasibility of CECI-SIM and determine the optimal system parameters, we conduct simulations of the image acquisition and reconstruction processes in CECI-SIM. Nine raw SIM images of tubulin in mouse embryonic fibroblast cells (NIH/3T3) recorded by a home-built SIM system are used as the ground truths. As can be seen in Figs. 2(a)–2(c), both CECI-SIM and HiFi-SIM can obtain detailed information of the tubulin sample, which are indistinguishable in the wide-field image. For quantitative assessment, we extract the intensity distribution along the red line in the blue enlarged box. As shown in Figs. 2(d)–2(f), four intensity peaks can be clearly distinguished from the intensity curves of HiFi-SIM and CECI-SIM, but are indistinguishable from the wide-field one. Furthermore, the intensity curve of CECI-SIM closely resembles that of HiFi-SIM, which means that the high frequency components are well extracted in CECI-SIM. Additionally, the corresponding frequency spectra of the CECI-SIM image beyond that of the wide-field image also confirm its super-resolution capability. This demonstrates that
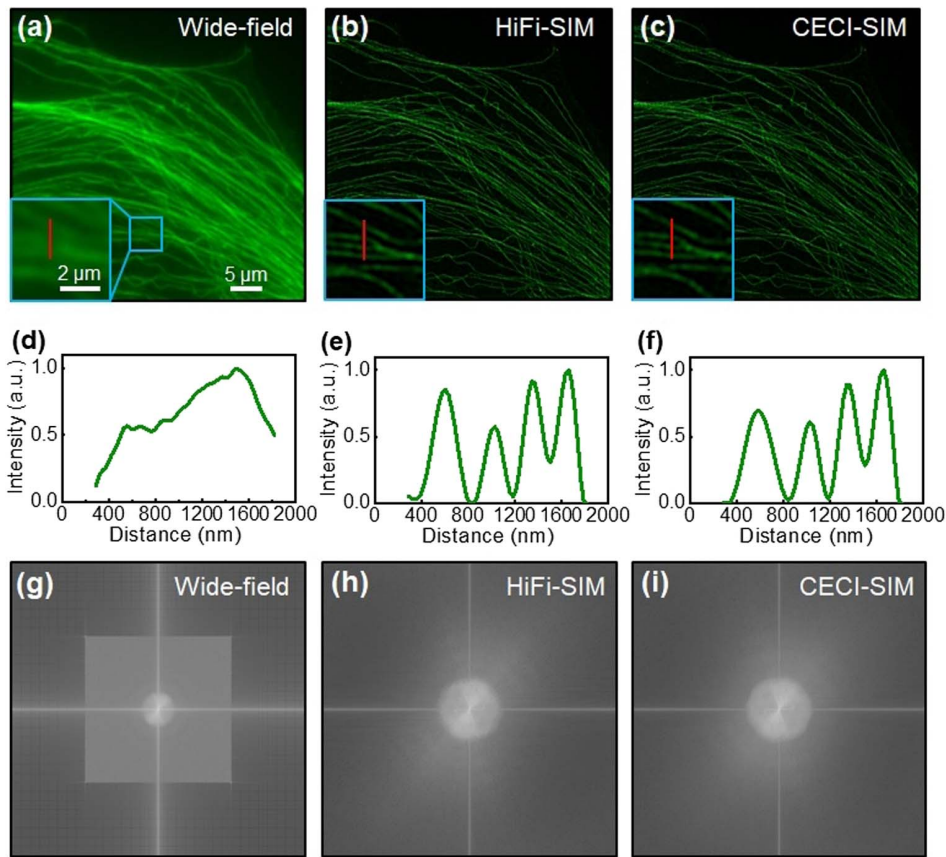
Fig. 2. Simulation results of CECI-SIM. (a)–(c) The wide-field, HiFi-SIM, and CECI-SIM images. (d)–(f) The intensity distributions along the red labeled line in the enlarged region of the images (a)–(c). (g)–(i) The corresponding frequency spectra of wide-field, HiFi-SIM, and CECI-SIM images.

CECI-SIM possesses a comparable super-resolution capability to conventional SIM, while achieving a threefold improvement in the imaging speed by reconstructing a single super-resolution image with only three compressed images.

Considering the high sensitivity of fluorescence microscopy systems to physical noise, it is necessary to assess the performance of CECI-SIM across various noise levels. To eliminate the influence of unknown noise in the ground truth, here we utilize an image containing artificially generated random curves. We simulate the image acquisition process of CECI-SIM and introduce additional Gaussian white noise with various standard deviations σ into the recorded data. Subsequently, we reconstruct the super-resolution images from the recorded data with various noise levels, as shown in Figs. 3(a)–3(f). Peak signal-to-noise-ratio (PSNR) and structural similarity (SSIM) of the reconstruction results are calculated to assess the quality of the reconstructed images. It can be seen from the blue enlarged boxes in Figs. 3(a)–3(f) that more and more background noises and artifacts appear in the reconstructed results of CECI-SIM as the noise increases. CECI-SIM exhibits robustness against the noise with a standard deviation below 0.1. However, further elevating noise levels will result in noticeable artifacts. When the noise standard deviation reaches 0.4, the line structures become almost indistinguishable, as shown in Fig. 3(f). The dependences of the PSNR and SSIM of the

reconstructed images on the standard deviation of the noise are presented in Figs. 3(g) and 3(h), which also show a decline of image quality with an increase in the noise. Despite the fact that the denoising modules are embedded in both the TCI and SIM reconstruction stages of CECI-SIM, achieving satisfactory results at high noise levels remains challenging.

4. EXPERIMENTAL RESULTS

The experimental arrangement of CECI-SIM is shown in Fig. 4(a). The beam from a continuous-wave laser with a wavelength of 532 nm (Laser Quantum, torus 532) is expanded by a beam expander (BE, Daheng Optics, GCO-2501) and then modulated by a high-speed digital micromirror device (DMD1, Texas Instruments, DLP6500), which is used to produce structured illumination patterns. A spatial filter (SF) is used to select only the ±1st order diffraction beams in three directions, allowing the generation of cosine fringes on the sample plane by interference. A polarization modulation module, consisting of a quarter-wave plate (QWP, Lbtek, MQWP20-532BM), a linear polarizer (LP, Thorlabs, LPVISA100-MP2), a half-wave plate (HWP, Thorlabs, WPH10M-532), and a partitioned half-wave plate (PHP, Lbtek, AHWP25-VIS-A-6P-M) is used to ensure that the polarization of the beam is parallel to the orientation of the fringes, which can obtain
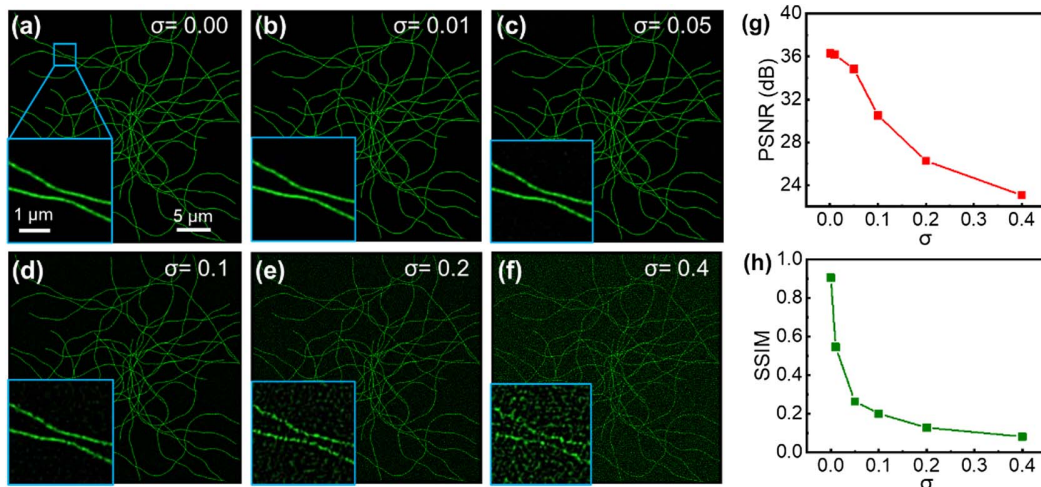
Fig. 3. Effect of noise on the image reconstruction of CECI-SIM. (a)–(f) The reconstructed images of CECI-SIM under additional Gaussian noise with different standard deviations. (g) and (h) The dependences of PSNR and SSIM of the reconstructed images on the noise standard deviation.
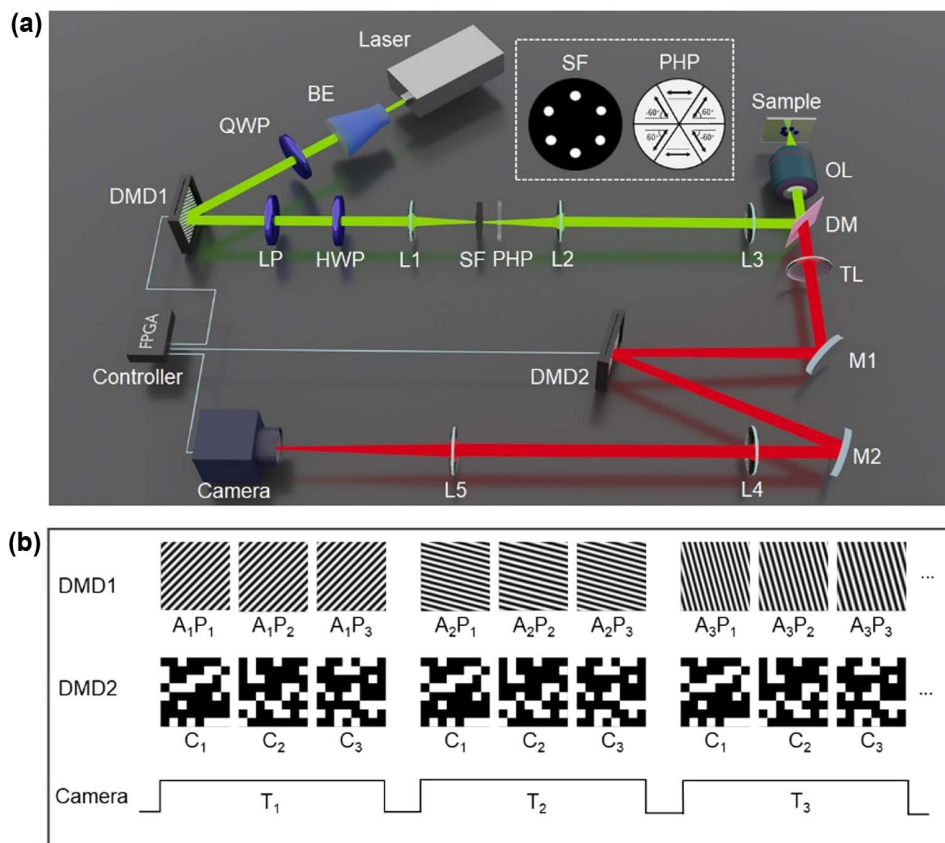
Fig. 4. Experimental arrangement of CECI-SIM. (a) The experimental arrangement of CECI-SIM. BE: beam expander; QWP: quarter-wave plate; LP: linear polarizer; HWP: half-wave plate; DMD1 and DMD2: digital micromirror devices; L1–L5: lenses; SF: spatial filter; PHP: partitioned half-wave plate; DM: dichromatic mirror; OL: objective lens; and TL: tube lens. (b) The time sequence of DMD1, DMD2, and the camera during the image acquisition of CECI-SIM.

the fringes with high contrast. After the beam is relayed by a $4f$ system consisting of a pair of lenses (L1 and L2), it is focused by an objective lens (OL, Olympus, UPLAPO100XOHR) and forms a structured illumination on the sample by interference.

The fluorescence signal generated by the structured light illumination is collected by the same objective lens, reflected by a dichroic mirror (DM, CHROMA, ZT532rdc), transmitted by a tube lens (TL), and then projected onto another digital
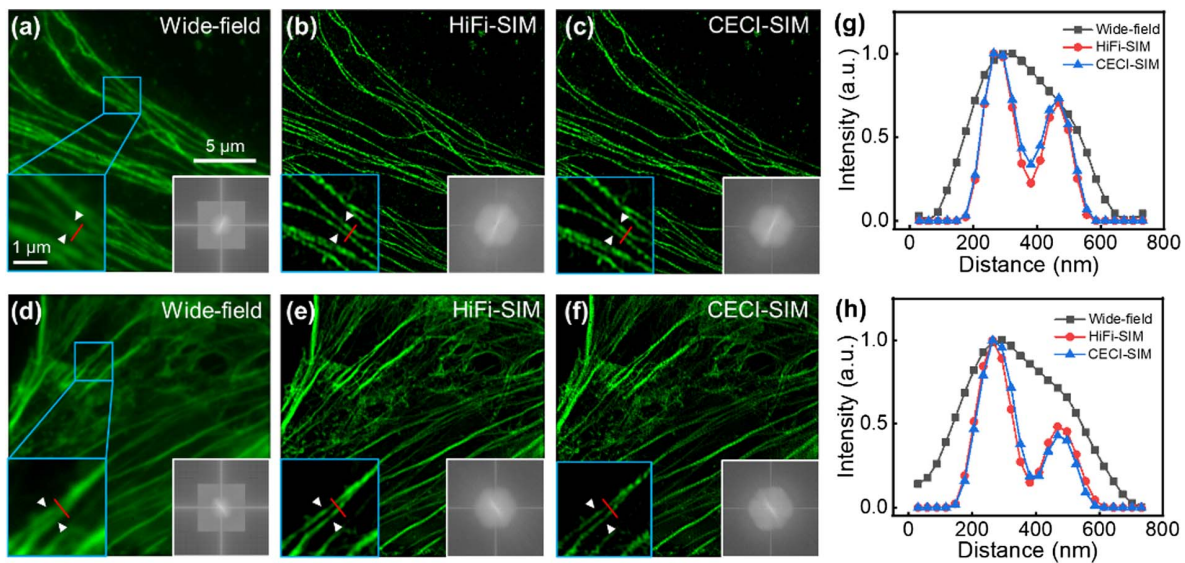
Fig. 5. (a)–(c) Wide-field, HiFi-SIM, and CECI-SIM images of tubulin in NIH/3T3 cells. (d)–(f) Wide-field, HiFi-SIM, and CECI-SIM images of actin in NIH/3T3 cells. The intensity distribution along the red labeled line in the wide-field (gray squares), HiFi-SIM (red balls), and CECI-SIM (blue triangles) images for tubulin (g) and actin (h).

micromirror device (DMD2, Texas Instruments, DLP6500) for spatial complementary encoding. Finally, the encoded fluorescence signal is transmitted by a $4f$ system consisting of a pair of lenses (L4 and L5) to a camera (Andor, Zyla5.5) for collection. Here, DMD1, DMD2, and the camera are triggered synchronously with a field programmable gate array (FPGA) controller. The structured illumination patterns of three phase-shift steps in every direction on DMD1 (A_iP_1, A_iP_2, A_iP_3, $i = 1, 2, 3$) are synchronized with a set of complementary codes (C_1, C_2, C_3) on DMD2, and the corresponding encoded images in every direction are integrated in every exposure (T_1, T_2, T_3) to obtain three compressed images, as shown in Fig. 4(b).

To demonstrate the feasibility of CECI-SIM on the super-resolution imaging of biological structures, we experimentally perform the observations of tubulin and actin in NIH/3T3 cells, which are important structures in cells, participating in the intracellular transport, cell mobility, and cell division. As shown in Fig. 4(a), a CECI-SIM system is built up to investigate the biological samples, which can also record the conventional SIM images by setting DMD2 as an all-reflection mode and recording the structured illuminated images one by one. The wide-field, HiFi-SIM, and CECI-SIM images of tubulin microtubules are shown in Figs. 5(a)–5(c), together with the enlarged region labeled with a blue box and the corresponding frequency spectra. It is obvious that both HiFi-SIM and CECI-SIM can distinguish the nearby tubulin microtubules clearly that cannot be distinguished in the wide-field image. The corresponding extended frequency spectra also confirm their super-resolution effect. The intensity distributions along the red labeled line are also extracted, as shown in Fig. 5(g). Two peaks with full width at half maximum (FWHM) of about 150 nm can be distinguished. The resolutions of the wide-field, HiFi-SIM, and CECI-SIM images of tubulin microtubule are estimated to be 261.6, 134.7, and 136.6 nm by the decorrelation analysis method [37]. As can be seen, CECI-SIM shows

the super-resolution performance close to that of HiFi-SIM, while possessing a threefold imaging speed.

Similarly, the actin microfilaments in the NIH/3T3 cells are also investigated with CECI-SIM. The wide-field, HiFi-SIM, and CECI-SIM images of actin microfilaments are shown in Figs. 5(d)–5(f), together with the enlarged region labeled with blue box and the frequency spectra. Again, the nearby actin microfilaments can be distinguished by both HiFi-SIM and CECI-SIM, while they are not distinguished in the wide-field image. The extracted intensity distributions along the red labeled line verify the close super-resolution performance, as shown in Fig. 5(h). Similarly, the resolutions of the wide-field, HiFi-SIM, and CECI-SIM images of actin microfilaments are also estimated by the decorrelation analysis, which are 262.8, 135.9, and 137.2 nm, respectively. In addition, CECI-SIM shows slightly more artifacts than HiFi-SIM, as shown in the enlarged regions in Figs. 5(g) and 5(h). Since actin microfilaments have denser distribution than tubulin microtubules, the reconstructed results are more vulnerable to artifacts due to calculation error. In general, these experimental results demonstrate that the super-resolution imaging capability of CECI-SIM is closed to that of HiFi-SIM, but with a threefold improvement in the imaging speed. Due to the information loss in the temporal compressive imaging and imperfect image reconstruction, the performance of CECI-SIM is inevitably slightly inferior to that of HiFi-SIM, but it is acceptable when considering the improved imaging speed. Besides, the image quality of CECI-SIM can be further optimized by aligning the hardware system more precisely and developing an image reconstruction algorithm with better performance.

5. CONCLUSIONS

In summary, we have developed a high-speed compressive structured illumination super-resolution microscopy (CECI-SIM) technique based on complementary encoding, improving

the super-resolution imaging speed threefold compared to conventional SIM. The high-speed super-resolution imaging capability was confirmed by theoretical simulations associated with the experimental observations of the tubulin and actin in mouse embryonic fibroblast cells. Since the time interval between the adjacent frames in CECI-SIM can be effectively shortened, the reconstruction artifacts induced by sample motion is depressed. With the higher imaging speed, CECI-SIM provides a powerful tool for detecting high-speed biological dynamics with fine details, such as organelle interactions [38], intracellular transports [39], and neural dynamics [40]. However, some drawbacks still exist in CECI-SIM. On the one hand, the additional spatial encoding process reduces the overall photon efficiency. Thus, the fluorescent labels with enough quantum efficiency and photostability are desired to ensure the SNR for the recorded images. On the other hand, the data compression ratio with complementary encoding in CECI-SIM is limited due to the reduced light throughput of the encoding mask, which makes it difficult to further improve the super-resolution imaging speed. Grayscale complementary encoding may be helpful to solve this problem [41]. Additionally, the strategy of CECI-SIM can also be applied to 3D SIM [42,43] and nonlinear SIM [44,45], where more structured illuminated images are required to recover the super-resolution images. Exploiting similar compressive measurement and reconstruction methods, high-speed super-resolution imaging with higher spatial resolution in longitudinal or transverse directions can be achieved.

APPENDIX A: METHODS

1. Cell Culture and Fluorescence Staining

The NIH/3T3 cell lines were purchased from Pricella Life Technology Co., Ltd. (Wuhan, China). NIH/3T3 cells were cultured in DMEM (Invitrogen, #11965-118) supplemented with 10% fetal bovine serum (FBS) (Gibco, #16010-159). To prevent bacterial contamination, 100 μg/mL penicillin and streptomycin (Invitrogen, #15140122) were added to the DMEM medium. Cells were grown under standard cell culture conditions (5% CO_2, humidified atmosphere at 37°C). NIH/3T3 cells were plated on a #1.5 glass-bottom dish over 48 h before sample preparation. For cell passage, cells were washed with pre-warmed PBS (Life Technologies, #14190500BT) three times and digested with 25% trypsin (Gibco, #25200-056) for 30 s. NIH/3T3 cell lines were tested for potential mycoplasma contamination (MycoAlert, Lonza),

and all tests showed negative results. Cells were grown on 35 mm, #1.5 glass coverslips [Standard Imaging (Beijing) Biotech, STGBD-035-1]. To increase cell adhesion, we pretreated glass-bottom dishes with fibronectin (Invitrogen, #33016015) for 1 h at 37°C. On the day of sample preparation, the cell density should be about 50%–70%. Cells were fixed with a 37°C pre-warmed fixation buffer for 10 min, containing 4% paraformaldehyde EMS and 0.1% glutaraldehyde in PBS. Then the sample was washed three times with PBS. For quenching the background fluorescence, we incubated the cells with 2 mL 0.1% $NaBH_4$ solution in PBS for 7 min. The sample was washed three times with 2 mL PBS and then incubated for 30 min in PBS containing 5% BSA (Jackson, #001-000-162) and 0.5% Triton X-100 (Fisher Scientific) at 37°C.

Tubulin staining. All antibodies were diluted in the 5% BSA + 0.5% triton solution described above. Next, we incubated the sample for 12 h with the appropriate dilution of primary antibodies: beta-tubulin (DSHB-E7) at 4°C. After primary antibodies incubation, the cells were washed 5 min with 2 mL PBS for three times. Secondary antibodies were incubated for 60 min with the appropriate dilutions of secondary antibodies (Cy3b secondary antibodies) at 25°C.

Actin staining. All dyes were diluted in the 5% BSA + 0.5% triton solution described above. Next, we incubated the sample for 40 min with the appropriate dilution of Acti-stain 555 phalloidin (Cytoskeleton, PHDH1-A) at 25°C. After washing three times with PBS, cells were fixed with post-fixation buffer for 10 min.

2. Imaging Reconstruction

The reconstruction of the simulation and experimental results is performed in the MATLAB (2022a) and PyCharm (2022.3.2) environments on a computer equipped with an Intel Core i7-10700 at 2.9 GHz CPU, 32 GB RAM, and NVIDIA GTX 1650 GPU. For the processing of three compressed images with a size of 512×512, the computation time is about 5 min.

APPENDIX B: COMPARISON OF ENCODING STRATEGIES

1. Comparison of Complementary and Pseudorandom Encoding

Simulations of CECI-SIM with complementary and pseudorandom codes are conducted to show the effect of encoding strategy on imaging performance. An image containing
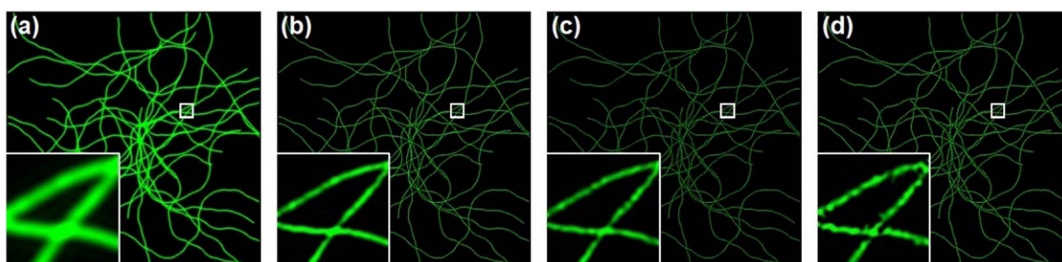
Fig. 6. (a)–(d) Wide-field, HiFi-SIM, and CECI-SIM images with complementary and pseudorandom codes. The insets are enlarged views of the regions marked with white boxes.

artificially generated random curves with a width of 32.5 nm is used as the ground truth. For the PSF calculation, the fluorescence wavelength is set as 560 nm, and the NA of the microscopy system is set as 1.5. After structured illumination, complementary codes and pseudorandom codes are utilized to encode the structured illuminated images, respectively. The final measurements are processed by the image reconstruction algorithm of CECI-SIM. The wide-field image, SIM image, and CECI-SIM reconstruction with complementary codes and pseudorandom codes are shown in Fig. 6. As can be seen from the insets, the reconstructed image with complementary codes has fewer artifacts than that with pseudorandom codes. Structured similarities of the reconstructed images are also calculated, which are 0.85 and 0.59 for complementary and pseudorandom codes, respectively. The complementary encoding strategy shows great superiority to pseudorandom encoding.

Disclosures. The authors have no conflicts to disclose.

Data Availability. Data underlying the results presented in this paper are available in Ref. [46].

REFERENCES

1. S. W. Hell and J. Wichmann, "Breaking the diffraction resolution limit by stimulated emission: stimulated-emission-depletion fluorescence microscopy," Opt. Lett. **19**, 780–782 (1994).
2. H. Blom and J. Widengren, "Stimulated emission depletion microscopy," Chem. Rev. **117**, 7377–7427 (2017).
3. D. Wildanger, R. Medda, L. Kastrup, *et al.*, "A compact STED microscope providing 3D nanoscale resolution," J. Microsc. **236**, 35–43 (2009).
4. E. Betzig, G. H. Patterson, R. Sougrat, *et al.*, "Imaging intracellular fluorescent proteins at nanometer resolution," Science **313**, 1642–1645 (2006).
5. M. J. Rust, M. Bates, and X. Zhuang, "Sub-diffraction-limit imaging by stochastic optical reconstruction microscopy (STORM)," Nat. Methods **3**, 793–795 (2006).
6. S. T. Hess, T. P. K. Girirajan, and M. D. Mason, "Ultra-high resolution imaging by fluorescence photoactivation localization microscopy," Biophys. J. **91**, 4258–4272 (2006).
7. M. G. L. Gustafsson, "Surpassing the lateral resolution limit by a factor of two using structured illumination microscopy," J. Micrsco. **198**, 82–87 (2000).
8. R. Heintzmann and T. Huser, "Super-resolution structured illumination microscopy," Chem. Rev. **117**, 13890–13908 (2017).
9. J. Demmerle, C. Innocent, A. J. North, *et al.*, "Strategic and practical guidelines for successful structured illumination microscopy," Nat. Protoc. **12**, 988–1010 (2017).
10. D. Li, L. Shao, B.-C. Chen, *et al.*, "Extended-resolution structured illumination imaging of endocytic and cytoskeletal dynamics," Science **349**, aab3500 (2015).
11. X. Huang, J. Fan, L. Li, *et al.*, "Fast, long-term, super-resolution imaging with Hessian structured illumination microscopy," Nat. Biotechnol. **36**, 451–459 (2018).
12. Q. Chen, X. Shao, P. Ling, *et al.*, "Quantitative analysis of interactive behavior of mitochondria and lysosomes using structured illumination microscopy," Biomaterials **250**, 120059 (2020).
13. A. V. Weigel, C. L. Chang, G. Shtengel, *et al.*, "ER-to-Golgi protein delivery through an interwoven, tubular network extending from ER," Cell **184**, 2412–2429 (2021).
14. F. Strohl and C. F. Kaminski, "Speed limits of structured illumination microscopy," Opt. Lett. **42**, 2511–2514 (2017).
15. F. Orieux, E. Sepulveda, V. Loriette, *et al.*, "Bayesian estimation for optimized structured illumination microscopy," IEEE Trans. Image Process. **21**, 601–614 (2012).
16. A. Lal, C. Shan, K. Zhao, *et al.*, "A frequency domain SIM reconstruction algorithm using reduced number of images," IEEE T. Image Process. **27**, 4555–4570 (2018).
17. S. Dong, J. Liao, K. Guo, *et al.*, "Resolution doubling with a reduced number of image acquisitions," Biomed. Opt. Express **6**, 2946–2952 (2015).
18. C. Ling, C. Zhang, M. Wang, *et al.*, "Fast structured illumination microscopy via deep learning," Photonics Res. **8**, 1350–1359 (2020).
19. W. Meiniel, P. Spinicelli, E. D. Angelini, *et al.*, "Reducing data acquisition for fast structured illumination microscopy using compressed sensing," in *Proceedings of the IEEE International Symposium on Biomedical Imaging* (IEEE, 2017), pp. 32–35.
20. B. Ozgurun and M. Cetin, "Compressed sensing structured illumination microscopy," in *Proceedings of the Annual International Conference of the IEEE Engineering in Medicine & Biology Society* (IEEE, 2020), pp. 1828–1831.
21. X. Yuan, D. J. Brady, and A. K. Katsaggelos, "Snapshot compressive imaging: theory, algorithms, and applications," IEEE Signal Process. Mag. **38**, 65–88 (2021).
22. Y. He, Y. Yao, D. Qi, *et al.*, "High-speed super-resolution imaging with compressive imaging-based structured illumination microscopy," Opt. Express **30**, 14287–14299 (2022).
23. R. G. Baraniuk, "Compressive sensing," IEEE Signal Process. Mag. **24**, 118–121 (2007).
24. R. G. Baraniuk, V. Cevher, M. F. Duarte, *et al.*, "Model-based compressive sensing," IEEE Trans. Inf. Theory **56**, 1982–2001 (2010).
25. P. Llull, X. Liao, X. Yuan, *et al.*, "Coded aperture compressive temporal imaging," Opt. Express **21**, 10526–10545 (2013).
26. M. Qiao and X. Yuan, "Coded aperture compressive temporal imaging using complementary codes and untrained neural networks for high-quality reconstruction," Opt. Lett. **48**, 109–112 (2023).
27. S. Boyd, N. Parikh, E. Chu, *et al.*, "Distributed optimization and statistical learning via the alternating direction method of multipliers," Found. Trends Mach. Learn. **3**, 1–122 (2010).
28. S. H. Chan, X. Wang, and O. A. Elgendy, "Plug-and-play ADMM for image restoration: fixed-point convergence and applications," IEEE Trans. Comput. Imaging **3**, 84–98 (2017).
29. X. Yuan, Y. Liu, J. Suo, *et al.*, "Plug-and-play algorithms for video snapshot compressive imaging," IEEE Trans. Pattern Anal. Mach. Intell. **44**, 7093–7111 (2022).
30. K. Zhang, Y. Li, W. Zuo, *et al.*, "Plug-and-play image restoration with deep denoiser prior," IEEE Trans. Pattern Anal. Mach. Intell. **44**, 6360–6376 (2022).
31. K. Zhang, W. Zuo, L. Zhang, *et al.*, "Deep plug-and-play super-resolution for arbitrary blur kernels," in *Proceedings of the IEEE/CVF Conference on Computer Vision and Pattern Recognition* (IEEE/CVF, 2019), pp. 1671–1681.
32. I. J. Myung, "Tutorial on maximum likelihood estimation," J. Math. Psychol. **47**, 90–100 (2003).
33. Y. Wang, J. Yang, W. Yin, *et al.*, "A new alternating minimization algorithm for total variation image reconstruction," SIAM J. Imaging Sci. **1**, 248–272 (2008).
34. A. Lal, C. Shan, and P. Xi, "Structured illumination microscopy image reconstruction algorithm," IEEE J. Sel. Top. Quantum Electron. **22**, 6803414 (2016).
35. X. Chen, S. Zhong, Y. Hou, *et al.*, "Superresolution structured illumination microscopy reconstruction algorithms: a review," Light Sci. Appl. **12**, 172 (2023).
36. G. Wen, S. Li, L. Wang, *et al.*, "High-fidelity structured illumination microscopy by point-spread-function engineering," Light Sci. Appl. **10**, 70 (2021).

37. A. Descloux, K. S. Grußmayer, and A. Radenovic, "Parameter-free image resolution estimation based on decorrelation analysis," Nat. Methods **16**, 918–924 (2019).

38. M. Schrader, L. F. Godinho, J. L. Costello, *et al.*, "The different facets of organelle interplay: an overview of organelle interactions," Front. Cell Dev. Biol. **3**, 56 (2015).

39. R. D. Vale, "The molecular motor toolbox for intracellular transport," Cell **112**, 467–480 (2003).

40. Y. Gong, C. Huang, J. Z. Li, *et al.*, "High-speed recording of neural spikes in awake mice and flies with a fluorescent voltage sensor," Science **350**, 1361–1366 (2015).

41. P. Wang, L. Wang, M. Qiao, *et al.*, "Full-resolution and full-dynamic-range coded aperture compressive temporal imaging," Opt. Lett. **48**, 4813–4816 (2023).

42. M. G. L. Gustafsson, L. Shao, P. M. Carlton, *et al.*, "Three-dimensional resolution doubling in wide-field fluorescence microscopy by structured illumination," Biophys. J. **102**, 13081–13086 (2005).

43. L. Schermelleh, P. M. Carlton, S. Haase, *et al.*, "Subdiffraction multicolor imaging of the nuclear periphery with 3D structured illumination microscopy," Science **320**, 1332–1336 (2008).

44. M. G. L. Gustafsson, "Nonlinear structured-illumination microscopy: wide-field fluorescence imaging with theoretically unlimited resolution," Proc. Natl. Acad. Sci. USA **102**, 13081–13086 (2005).

45. H. Zhang, M. Zhao, and L. Peng, "Nonlinear structured illumination microscopy by surface plasmon enhanced stimulated emission depletion," Opt. Express **19**, 24783–24794 (2011).

46. Z. Huang, "Data for CECI-SIM," https://figshare.com/articles/dataset/DATA_CECI-SIM_rar/25049927 (2024).